Electron-impact excitation of the Rb $7\,^2S_{1/2}$, $8\,^2S_{1/2}$, $5\,^2D_{3/2}$, and $6\,^2D_{3/2}$ states

Zuyi Wei, Connor Flynn, Aaron Redd, and Bernhard Stumpf
Department of Physics, University of Idaho, Moscow, Idaho 83843
(Received 2 October 1992)

Electron-impact cross sections for excitation of the $7\,^2S_{1/2}$, $8\,^2S_{1/2}$, $5\,^2D_{3/2}$, and $6\,^2D_{3/2}$ states of rubidium have been measured from threshold to 1000 eV. The optical-excitation-function method has been employed in a crossed atom- and electron-beam apparatus. Relative, total (cascade including) experimental cross sections are made absolute by comparison with the known total cross section of the Rb $D1$ line. Total excitation cross sections are compared with theoretical calculations employing first Born approximation and theoretical branching ratios. Born cross sections for the $7\,^2S_{1/2}$ and $8\,^2S_{1/2}$ states are obtained from the literature, while Born cross sections for the $5\,^2D_{3/2}$, $6\,^2D_{3/2}$, and all cascading states are calculated in this paper. At high energies, the measured total $^2D_{3/2}$ state cross sections show $1/E$ behavior and converge to first Born theory; for $E > 100$ eV, experiment and theory agree within 6.7% for $5\,^2D_{3/2}$ and within 3.7% for $6\,^2D_{3/2}$. The total cross sections for the $^2S_{1/2}$ states do not converge to Born theory even at 1000 eV, and it is shown that this cannot be attributed to cascading. At low energies, $^2S_{1/2}$ and $^2D_{3/2}$ state total excitation cross sections have similar shapes with sharply peaked maxima at about 0.9 eV above threshold. After cascading is corrected using first Born theory, estimated experimental cross sections for direct excitation of higher fine-structure states of rubidium are given.

PACS number(s): 34.80.Dp

I. INTRODUCTION

Atomic collision experiments have used alkali-metal atoms to test and suggest theoretical advances ever since the very beginning of quantum theory. Unlike hydrogen-metal elements, alkali are monatomic in the gas phase and do not have degenerate excited states. Yet they are still relatively simple atoms being well described by one electron in the field of a spherical core. Furthermore, characteristic for all alkali-metal atoms is the strong coupling between the S ground state and the first excited P state. The lowest P state alone accounts for over 97% of the static dipole polarizability of an alkali-metal atom, while in hydrogen all bound states together account for only 81%. Close-coupling or R-matrix theory is therefore ideally suited to describe elastic and first-excited-state inelastic electron–alkali-metal-atom scattering, since the inclusion of higher states has only little effect on the results of calculations for these two types of scattering processes.

The first effort, to our knowledge, to develop a precision close-coupling theory for electron scattering on alkali-metal atoms was made by Moores and Norcross [1] in 1971. Sodium was chosen as a target since core polarization has only minor and spin-orbit interaction negligible influence on the collision process. This pioneering work was followed by a host of electron-sodium collision experiments during the past 20 years. For lack of a general review, some are listed here: total [2,3], differential elastic and inelastic [4–12], and angular-integrated inelastic [13–17] cross sections have been measured. Collisions with polarized atoms or electrons [18,19] have been studied, photon-electron coincidence experiments [20–22] have been performed, and electron impact of laser-excited sodium $3P$ atoms [17,23–32] has been investigated.

In contrast, relatively little work has been done on the heavy alkali-metal atoms rubidium and cesium. Using the atomic-recoil technique, total cross sections have been measured by Visconti, Slevin, and Rubin [33] for Rb and Cs at electron energies 0.3–9 eV and, more recently, by Jaduszliwer and Chan [34] for Cs at 2–18 eV. Gehenn and Reichert [35] have studied relative, elastic, and $6\,^2P_{1/2,3/2}$ inelastic differential cross sections in cesium for energies 0.8–20 eV. Also in Cs, Klewer, Beerlage, and Van der Wiel [36] have obtained the polarization and angular distribution of elastically scattered electrons at 13–25 eV. Chen and Gallagher [37] have measured total cross sections and linear light polarizations of Rb and Cs resonance lines at energies from threshold to 1000 eV. More recently, Naβ *et al.* [38] have studied the circular light polarization of the Na, K, Rb, and Cs resonance lines excited by longitudinally polarized electrons from threshold to 6 eV, and Eschen *et al.* [39] have performed similar experiments on Cs with transversely polarized electrons. The relative lack of electron-collision experiments with the heavy alkali-metal atoms can probably be attributed to the fact that until recently no accurate theoretical calculations were available, the difficulty being that strong core polarization and spin-orbit interaction need to be considered. Meanwhile, however, Thumm and Norcross [40–42] have developed a relativistic R-matrix theory for electron collisions with cesium that promises to be as accurate for the heavy alkali-metal atoms as the work by Moores and Norcross [1] for sodium. Thus far, results by Thumm and Norcross include, up to 2.8 eV energy, angular-integrated elastic and inelastic cross sections, the latter for $6\,^2P_{1/2}$, $6\,^2P_{3/2}$, $5\,^2D_{3/2}$, and $5\,^2D_{5/2}$ excitation [40], a careful study of near-threshold resonances [41], and differential and momentum-transfer cross sections [42].

In light of this recent strong theoretical interest in elec-

tron collisions with heavy alkali-metal atoms, we have measured the electron-impact cross sections for the $7\,^2S_{1/2}$, $8\,^2S_{1/2}$, $5\,^2D_{3/2}$, and $6\,^2D_{3/2}$ states of rubidium, using the optical-excitation-function method in a crossed atom- and electron-beam apparatus. Energy levels and transitions are shown in Fig. 1. The optical-excitation-function method yields an angular-integrated, cascade-including cross section, which we refer to, following earlier convention [17], as total cross section Q_T. After correcting for cascading, the direct cross section Q_D is obtained, which corresponds to the angular-integrated theoretical cross section. We have chosen the above four higher rubidium states for the following reasons: The total cross section for the Rb $5P$ state has already been measured [37], and calculations for this state based upon the work in Refs. [40–42] are forthcoming. For higher-state excitation, however, the situation is more difficult. The close-coupling method converges rapidly for elastic and first-excited-state inelastic scattering, but calculations for higher states are expected to be very sensitive to the number and type of neighboring states included. Furthermore, the thresholds [44] of the $7\,^2S_{1/2}$, $8\,^2S_{1/2}$, $5\,^2D_{3/2}$, and $6\,^2D_{3/2}$ states are at 3.262, 3.601, 3.186, and 3.557 eV, while the thresholds for $7\,^2P_{1/2}$, $7\,^2P_{3/2}$, $8\,^2P_{1/2}$, and $8\,^2P_{3/2}$ are at 3.451, 3.455, 3.699, and 3.701 eV. Given these small energy spacings between states of different parity, one can therefore expect that the colliding electron couples these states strongly at large impact parameters. Higher-state excitation is thus a true multistate problem, which is not yet well handled by theory.

Since the cross sections for optically forbidden higher states are much weaker and hence more difficult to measure than cross sections for the first excited P state, experimental information on higher-state excitation is sparse. Zajonc and Gallagher [45] have investigated electron-impact excitation of the Li $3S$, $4S$, $3D$, and $4D$ states from threshold to 1000 eV, and Lin and co-workers have extensively studied higher-state excitation of sodium [16] and potassium [46] from threshold to about 150 eV.

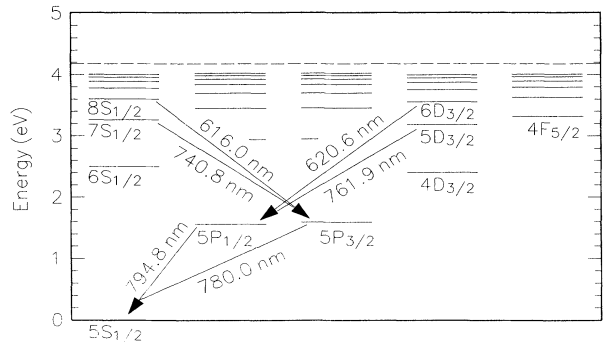

FIG. 1. Energy levels and spectral lines of rubidium. The electron-impact cross sections of the $7\,^2S_{1/2}$, $8\,^2S_{1/2}$, $5\,^2D_{3/2}$, and $6\,^2D_{3/2}$ states are measured by optical detection of the 740.8-, 616.0-, 761.9-, and 620.6-nm spectral lines. Cascading into the $7\,^2S_{1/2}$ and $8\,^2S_{1/2}$ states is from the $n\,^2P_{1/2,3/2}$ states, while cascading to the $5\,^2D_{3/2}$ and $6\,^2D_{3/2}$ states is due to the $n\,^2P_{1/2,3/2}$ and $n\,^2F_{5/2}$ states.

While these measurements show systematic trends for a given term series of a given atom, no general higher-state pattern across the alkali-metal atoms has yet evolved.

The energy range covered by our experiment is from threshold to 1000 eV. Measurements at high energies ($\sim$100–1000 eV) are necessary to check whether the cross sections converge to calculations in first Born approximation. Only if such convergence is established are comparisons between experimental data and first Born theory in the intermediate- and low-energy ranges conclusive. Data taken between $\sim$10–100 eV assist the development of electron-atom collision theories in the intermediate-energy range [47–49], a topic of considerable current interest. Measurements at low energies are crucial for future R-matrix calculations. The issue here is not so much to provide an experimental test for the convergence of partial waves, for which differential scattering experiments are more appropriate, but rather to help decide which states should be included in the target description.

II. EXPERIMENT

Figure 2 shows a diagram of the apparatus in the plane of the electron and atom beam which intersect each other at right angles. Observation of the electron-impact-produced atomic-line radiation is made along the third, orthogonal axis. Figure 3 illustrates the detection optics; a cross-sectional view in the plane of atom beam and the axis of optical detection is given. As indicated in Figs. 2 and 3, we are using a right-hand Cartesian coordinate system with origin in the center of the interaction region to describe directions.

The electron and atom-beam system is housed in an all

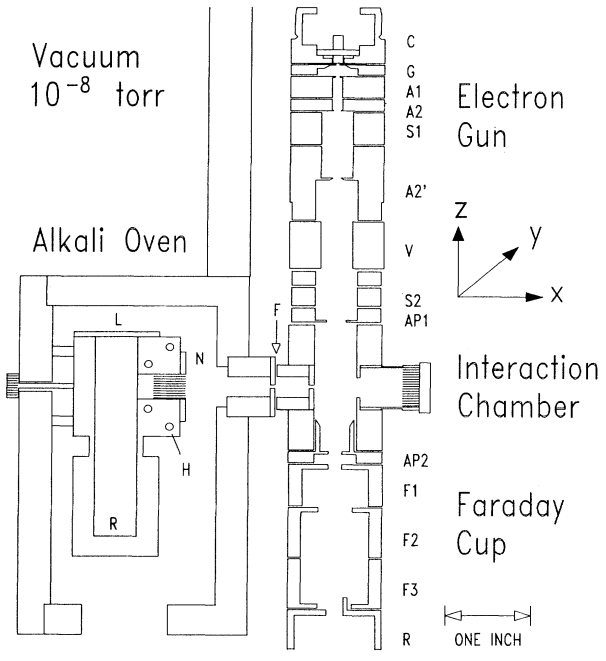

FIG. 2. Cross-sectional view of the apparatus in the plane formed by electron and atom beam (in scale).

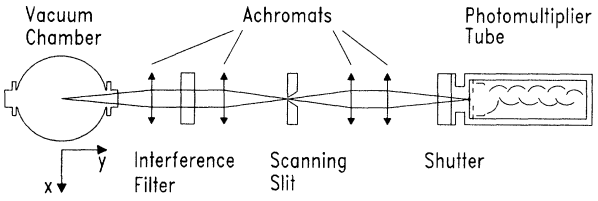

FIG. 3. Cross-sectional view of the apparatus in the plane formed by atom beam and axis of optical detection (optical distances and angles are to scale).

304-stainless-steel chamber, evacuated by a 200-l/s turbopump. With a moderate bakeout of 120 °C, a base pressure of 1×10^{-9} Torr is obtained. The chamber is carefully shielded with mu-metal, and only nonmagnetic materials are used inside the vacuum chamber and in the surrounding detection optics. Electron-beam and atom-beam components are demagnetized to remove residual magnetism from machining. As a result, the magnetic field inside the chamber is measured to be no more than 5 mG and, as we show below, the electron beam is not observably influenced by magnetic fields.

A. Electron beam

The axially symmetric electron gun is built following an earlier electron-optical design described by Stumpf and Gallagher [17]. Electrons are generated by an indirectly heated oxide cathode C and controlled by a grid G with Pierce geometry. The distance between cathode and grid is adjusted such that the electron current is optimized at low energies. The beam is accelerated by anodes $A1$ and $A2$, and focused into the interaction region by a lens formed by elements $A2'$, V, and aperture 1 (AP1). Element $A2'$ is at the same potential as anode $A2$. The position of the electron beam can be changed along the directions of atom beam (x axis) and of optical detection (y axis) by two sets of steering units $S1$ and $S2$. Aperture 1 and aperture 2, before and after the interaction chamber, are used to optimize and monitor electron-beam performance. Both apertures and the interaction chamber are at ground potential. The Faraday cup is segmented, consisting of three elements $F1$, $F2$, and $F3$, and terminated by a reflector electrode R. The Faraday segments are positively biased, at about 25 V, with respect to the interaction chamber in order to increase collection efficiency. The reflector is held at cathode potential and has a half-cylinder on top. The resulting asymmetric electric field deflects electrons to the walls of the Faraday cup, preventing them from traveling back to the interaction chamber. About 90% of the current entering the Faraday cup is collected at the last segment $F3$ while the remaining 10% is collected by segments $F1$ and $F2$. An opening in the reflector electrode is provided for an incoming laser beam in future collision studies with laser-excited rubidium atoms.

Size and position of the electron beam in the interaction region are determined by scanning the image of the electron-impact-produced 780-nm-resonance fluorescence along the atom-beam direction (x) with a slit of 0.25 mm width (Δx) and 1 mm height (Δz). Electron-beam profiles were taken at energies of 2.5, 3.5, 4.5, 5.5, 10.5, 20.5, 50.5, 100.5, 400.5, and 1000.5 eV, and results for energies of 3.5 and 100.5 eV are shown in Fig. 4. The x position in Fig. 4 is obtained from a micrometer reading (±0.005 mm) at the scanning slit, divided by the 0.70 optical magnification, and the origin $x=0$ (±0.1 mm) is defined by the position of the optical detection axis. As can be seen, the measured electron-beam profiles are centered at this position within 0.1 mm, independent of energy. No electron-beam steering was used to achieve this result. This implies that residual electric and magnetic fields have negligible effect on the electron-beam path. Furthermore, the width (Δy) of the atom beam is approximately 5 mm in the interaction region and the electron beam has a circular cross section. We can therefore deduce from the data in Fig. 4 that $\approx99.9\%$ of the electron current at 3.5 eV traverses the atom beam. Since we find that the electron-beam diameter decreases with increasing energy, we state the systematic error due to incomplete overlap of electron and atom beam as $\approx0.1\%$ for all electron energies considered.

The total current passing through the atom beam is collected as the sum of the currents to aperture 2 and the Faraday cup. Roughly, this current is 0.1–1 μA for energies 1–10 eV, 1–10 μA for energies 10–100 eV, and 10–50 μA for energies 100–1000 eV. The current to aperture 2 is a fraction of about 5×10^{-2} for energies below 10 eV, 5×10^{-4} at 100 eV, and 5×10^{-5} at 1000 eV. Loss of collection efficiency due to electron reflection at aperture 2 at low energies was measured to be about (30±10)%, so a correction ($\approx1.5\%$) was made in evaluating the total current. Loss of collection efficiency due to electron reflection within the Faraday cup was found to be negligible. This was checked by varying the positive-bias voltage to Faraday segment $F1$ and observing that the total current collected by aperture 2 and the Faraday cup remained constant. This also suggested that no low-energy secondary electrons traveled from within

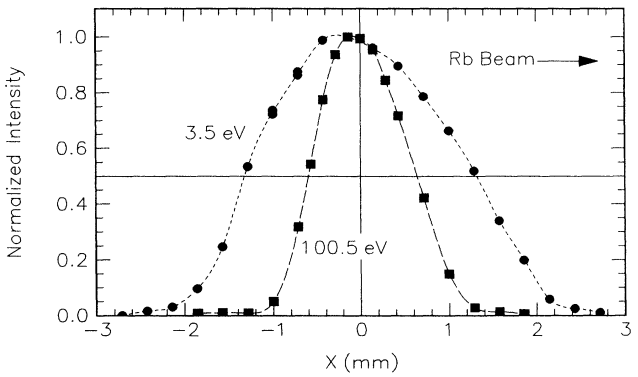

FIG. 4. Electron-beam profiles, measured by scanning the image of the electron-impact-produced 780-nm resonance fluorescence along the atom-beam direction (x). Experimental data are normalized to unity at $x=0$, the position of the axis of optical detection. Results are shown for electron energies of 3.5 eV (●) and 100.5 (■). The full widths at half maximum are 2.6 and 1.2 mm. The direction of the rubidium beam is shown.

the cup to the interaction region. On the other hand, low-energy secondary electrons originating from aperture 2 could be a problem, since the cross sections reported in this paper have sharply peaked maxima Q_{max} at energies between 4 and 5 eV and fall off rapidly with increasing energy. Thus, low-energy secondary electrons entering the interaction region could falsify the high-energy tail of the cross sections. However, as stated above, the current collected on aperture 2 was typically 5×10^{-4} of the total current at 100 eV and 5×10^{-5} of the total current at 1000 eV. From the cross-section data reported in Sec. III D we have $Q_T(100\text{ eV})/Q_T(\text{max})=0.095$, 0.087, 0.063, 0.066, and $Q_T(1000\text{ eV})/Q_T(\text{max})=0.012$, 0.011, 0.0064, 0.0067, for $7\,^2S_{1/2}$, $8\,^2S_{1/2}$ and $5\,^2D_{3/2}$, $6\,^2D_{3/2}$, respectively. A possible contribution by low-energy secondary electron excitation to the high-energy cross-section data is thus no more than 1%.

The energy E of the electron beam in the interaction region is given by the cathode voltage V corrected for a contact potential C which we define such that $E=|V|+C$. This contact potential can vary in time due to alkali-metal atom buildup in the interaction chamber. We therefore let the atom beam run for several hours before taking data, presumably creating a homogeneous alkali-metal layer in the interaction chamber (at room temperature). This procedure resulted in a contact potential that was constant in time. Its average value for all data runs reported in this paper is 0.47 ± 0.16 eV, and changes during individual data runs are about 0.1 eV. Each data run was corrected for its own individual contact potential by extrapolating a linear least-squares fit through the data points immediately above threshold to zero signal. This determined the experimental threshold and thus the contact potential since the true threshold energy is well known. The optically forbidden transitions considered in this paper have very steep onsets at threshold and the below-threshold signal due to the finite energy spread of the electron beam is thus easily recognized. This makes our energy calibration fairly accurate, $\Delta E<0.05$ eV. In addition, the accuracy of setting and stability of the cathode voltage is $10^{-4}E$ as specified by the manufacturer and confirmed in our laboratory with a precision $5\frac{1}{2}$-digit voltmeter. Obviously, this has negligible effect on the data reported. In summary, we state the energy uncertainty of individual data points as 0.1 eV due to contact-potential drifts. In addition, an uncertainty of less than 0.05 eV affects the entire energy scale of each reported cross section due to the limited accuracy in determining the experimental threshold.

Electron-energy distributions were measured at several energies between 1 and 10 eV using aperture 2 and Faraday segment $F1$ as a retarding analyzer. Figure 5 shows the result at an energy of 3.10 eV: A full width at half maximum $\Delta E_{1/2}=0.25$ eV is obtained, corresponding to a thermal distribution at 1140 K. Space-charge corrections [50] to beam energy and energy distribution are negligible at the low currents employed here. For example, at an energy of 3 eV and a current of 0.5 μA the potential drop from the inner wall of the interaction chamber (radius 6.35 mm) to the edge of the electron beam (radius ≈1.3 mm) is only about 14 mV, while the potential drop from the edge to the center of the beam is about 4 mV.

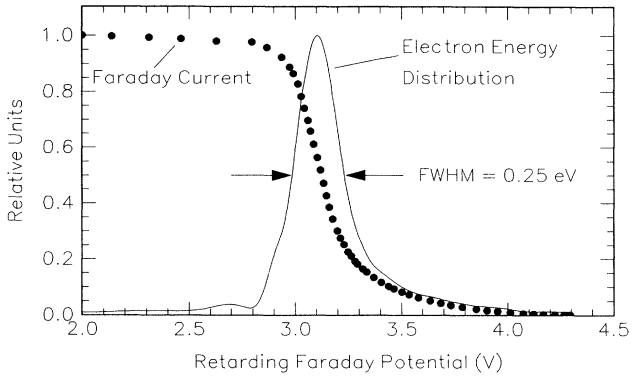

FIG. 5. Measured Faraday current in relative units (●) as a function of a retarding Faraday potential in volts. The solid curve, obtained by numerical differentiation of the experimental data, represents the electron-energy distribution. The full width at half maximum (FWHM) of the electron-energy distribution is 0.25 eV.

B. Atom beam

As shown in Fig. 2, the alkali-metal oven is mounted in a water-cooled chamber in order to avoid alkali-metal contamination of the electron-beam system. The oven is machined from 304 stainless steel and consists of an unheated reservoir (R) at the bottom and of a heated nozzle (N) at the top. Reservoir and nozzle are thermally separated to minimize dimer formation. The oven is loaded from the top in an argon atmosphere with 99.9% pure rubidium. The oven lid (L) as well as the removable nozzle unit are sealed with nickel-plated ultrahigh-vacuum gaskets. Four rod heaters (H) are employed, each heater consisting of two insulated wires with current in opposite directions. The magnetic field of these heaters is only a few milligauss in the center of the interaction chamber and, as shown above, it does not cause any measurable beam deflection.

Typical temperatures, measured with chromel-constantan thermocouples, are 132 °C at the nozzle and 122 °C at the reservoir. Using this temperature gradient and the thermokinetical data of Lapp and Harris [51], we estimate the concentration of rubidium dimers to be 0.06% in the nozzle region. The nozzle is formed by about 60 304-stainless-steel tubes of 0.6 mm inner diameter and 8.2 mm length. Thus the ratio of the mean free path Λ, the tube length L, and the tube diameter $2r$ is roughly $\Lambda:L:2r=100:10:1$. It follows that tube geometry and oven temperature are such that the flow through the nozzle is in the transparent mode [52], where only wall collisions occur and atom-atom collisions are negligible. This is important since it allows us to infer that the low dimer concentration within the oven remains essentially the same in the atom beam.

The atom beam is shaped by two 4×1-mm^2 collimating apertures and collected by a honeycomb condenser. In the interaction region, the width (Δy) of the atom

beam is 5 mm, and its thickness (Δz) is 1.2 mm. A beam flag (F), controlled by a linear-motion feedthrough, turns the atom beam on and off. By taking data with and without atom beam all background signals, including electron-impact-produced fluorescence from residual gas molecules, are subtracted from the optical signal. Oven light, which would not be subtracted out by this chopping method, is unmeasurably small. Condensation, mostly on the first collimating aperture, reduces the thickness of the atom beam during the time of a data run ($\approx$36 hrs). This leads to a signal drop of about 3% per hour which is monitored by measuring the current-normalized optical signal at 100 eV about every 15 min. Since we find that the signal drop is a smooth, linear function of time, we do not consider the time correction that we apply to the data an additional source of error.

C. Detection optics

Light from the intersection of atom beam and electron beam is collected by $f/5$ optics and imaged into the plane of a scanning slit. As described in Sec. II A, the scanning slit is used to measure the spatial profile of the electron beam; it is removed while cross-section data are taken. The plane of the scanning slit is imaged onto the cathode of a cooled photomultiplier, followed by a standard photon-counting system.

As shown in Fig. 3, interaction region, scanning slit, and photocathode are in conjugate focal planes. Antireflection-coated achromats with 4 cm diameter and focal lengths 20, 14, 14, and 18 cm are employed. Alignment of the detection optics is carried out with a He-Ne laser and a precision pinhole in the interaction region. Wavelength selection is with interference filters of three-cavity design; suppression of adjacent spectral lines is better than 0.1%. Filter transmissions and cathode quantum efficiencies will be given in Sec. III B, where they will be used for absolute calibration of cross sections. The GaAs cathode of the photomultiplier has a 650S response, an area 10×10 mm^2, and is cooled at -30 °C. Fine positioning of the photomultiplier cathode is done by maximizing the 100-eV signal of the Rb D_2 line. The spatial dependence of the cathode sensitivity was carefully measured replacing the scanning slit by a pinhole of 0.25 mm diameter with a diffuse white-light source in front. Based on these measurements, we can safely estimate that integrated sensitivities for low- and high-energy signals, with electron-beam shapes as depicted in Fig. 4, differ by no more than 1%.

III. RESULTS

The measured quantity in this experiment is $I(90°;\lambda)/i$, where $I(90°;\lambda)$ is the intensity of a spectral line of wavelength λ with upper state nlj emitted in a direction perpendicular to the electron beam and i is the total current passing through the atom beam. $I(90°;\lambda)/i$ is proportional to the angular-integrated cross section $Q_D(nlj)$ for "direct" electron-impact excitation of the state nlj provided corrections are made for cascading and fluorescence anisotropy. We define a cascade cross section

$$Q_C(nlj)=\sum_{n',l',j'} Q(n'l'j')B(n'l'j'\rightarrow nlj)\ , \tag{1}$$

where $B(n'l'j'\rightarrow nlj)$ is the branching ratio of a higher state $n'l'j'$ into the state nlj, and denote the linear polarization of the spectral line λ by $P(\lambda)$ (%). Then the total, that is, the cascade-including cross section $Q_T(nlj)$ for electron-impact excitation of state nlj, is given by [43]

$$\begin{aligned} Q_T(nlj)&=Q_D(nlj)+Q_C(nlj)\\ &=k[1-P(\lambda)/300]I(90°;\lambda)/i\ , \end{aligned} \tag{2}$$

where k is an experimental constant.

A. Polarization

Radiation from states with zero orbital angular momentum is isotropic and hence the linear polarization of the 740.82- and 615.96-nm spectral lines originating from the $7\,^2S_{1/2}$ and $8\,^2S_{1/2}$ states vanishes. Radiation from the $5\,^2D_{3/2}$ and $6\,^2D_{3/2}$ states, however, is partially polarized. We estimate it as follows. The lifetimes of the $5\,^2D_{3/2}$ and $6\,^2D_{3/2}$ states have been calculated by Theodosiou [53] as 240 and 251 ns, in good agreement with experiment [54,55]. Measured hyperfine splitting constants are 4.18 MHz [54] and 2.28 MHz [56] for ^{85}Rb, and 14.4 MHz [54] and 7.84 MHz [57] for ^{87}Rb. The corresponding hyperfine relaxation times of the $5\,^2D_{3/2}$ and $6\,^2D_{3/2}$ states are 38 and 70 ns (^{85}Rb), and 11 and 20 ns (^{87}Rb). Thus the hyperfine structure in these $^2D_{3/2}$ states is fully resolved, leading to fairly isotropic decay. We therefore let $1-P(\lambda)/300\approx1$ in Eq. (2) and assume that the error associated with this approximation is no more than a few percent. A preliminary measurement of the linear polarization of the $5\,^2D_{3/2}\rightarrow5\,^2P_{1/2}$ and $6\,^2D_{3/2}\rightarrow5\,^2P_{1/2}$ fluorescence from threshold to 1000 eV confirmed that estimate.

B. Normalization

For negligible polarization correction, the constant k in Eq. (2) converts the measured signal $I(90°;\lambda)/i$ in units of counts/(sμA) into the total cross section $Q_T(nlj)$ in units of πa_0^2. While k is an experimental constant, it is extremely difficult to determine experimentally, especially in a crossed-beam configuration where an absolute measurement of the atom-beam density would have to be made. We have therefore used an alternative method to obtain an absolute total cross section $Q_T(nlj)$ from the measured $I(90°;\lambda)/i$ by referencing our data to the well-known [37] cross section Q_T of the rubidium D_1 line. Specifically, we determine at a fixed energy the ratio of intensities $S(\lambda)$ and $S(794.8\text{ nm})$ and then express $Q_T(nlj)$ in terms of $Q_T(^2P_{1/2})$:

$$\begin{aligned} Q_T(nlj)=Q_T(5\,^2P_{1/2})&\frac{E(794.8\text{ nm})T(794.8\text{ nm})}{E(\lambda)T(\lambda)B(\lambda)}\\ &\times\frac{S(\lambda)}{S(794.8\text{ nm})}\ . \end{aligned} \tag{3}$$

$E(\lambda)$, $T(\lambda)$, and $B(\lambda)$ denote cathode quantum efficiencies, interference-filter transmissions, and branch-

ing ratios. Filter transmissions $T(\lambda)$, measured with an accuracy $\Delta T = \pm 1\%$, are

70.4% at 615.96 nm ($8\,^2S_{1/2} \rightarrow 5\,^2P_{3/2}$),
70.0% at 620.63 nm ($6\,^2D_{3/2} \rightarrow 5\,^2P_{1/2}$),
53.4% at 740.82 nm ($7\,^2S_{1/2} \rightarrow 5\,^2P_{3/2}$),
63.4% at 761.89 nm ($5\,^2D_{3/2} \rightarrow 5\,^2P_{1/2}$),
and 54.7% at 794.76 nm ($5\,^2P_{1/2} \rightarrow 5\,^2S_{1/2}$).

Estimated cathode quantum efficiencies $E(\lambda)$ are 12.67% (616.0 nm), 12.64% (620.6 nm), 11.59% (740.8 nm), 10.98% (761.9 nm), and 9.52% (794.8 nm). The ratios $E(794.8\text{ nm})/E(\lambda)$ needed in Eq. (3) are probably accurate within 10%. We assess the same level of accuracy to the branching ratios $B(\lambda)$, obtained from Theodosiou [58], $B(616.0\text{ nm}) = 0.338$, $B(620.6\text{ nm}) = 0.618$, $B(740.8\text{ nm}) = 0.392$, and $B(761.9\text{ nm}) = 0.470$. $B(794.8\text{ nm}) = 1$ is omitted in the numerator of Eq. (3). Measurements are carried out at a fixed energy of 100.5 eV, and interference filters for the Rb D_1 line and for the other spectral line of wavelength λ are quickly interchanged. From the experiment of Chen and Gallagher [37] we have at 100.5 eV $Q_T(5\,^2P_{1/2}) = 7.75 \pm 0.55 \pi a_0^2$ where the error includes a 6% uncertainty in the normalization of the cross-section scale. Chen and Gallagher give $Q_T(5\,^2P)$ for the unresolved P state; we have used an oscillator-strength ratio of 2.033 [59] to obtain $Q_T(5\,^2P_{1/2})$. The measured intensity ratios $S(\lambda)/S(794.8\text{ nm})$ are $0.003\,21 \pm 0.000\,36$ at 616.0 nm, $0.002\,80 \pm 0.000\,56$ at 620.6 nm, $0.005\,86 \pm 0.000\,24$ at 740.8 nm, and $0.006\,77 \pm 0.000\,47$ at 761.9 nm. Using Eq. (3), we thus obtain, at an energy of 100.5 eV, $Q_T(7\,^2S_{1/2}) = 0.0975 \pm 0.0132 \pi a_0^2$, $Q_T(8\,^2S_{1/2}) = 0.0430 \pm 0.0073 \pi a_0^2$, $Q_T(5\,^2D_{3/2}) = 0.0835 \pm 0.0125 \pi a_0^2$, and $Q_T(6\,^2D_{3/2}) = 0.0207 \pm 0.0050 \pi a_0^2$. Errors are the geometrical mean of relative errors in Eq. (3), multiplied with Q_T.

C. Cascading

In order to estimate cascading according to (2) and (1), we calculate $Q_T(nlj)$ in first Born approximation, obtain the ratio of the direct and the total cross section $Q_D(nlj)/Q_T(nlj)$, and multiply the experimental $Q_T(nlj)$ by this fraction to obtain an estimated experimental direct cross section $Q_D(nlj)$. Of course, we also use these calculations for comparison with the experimental data. Experimental total and estimated experimental direct cross sections are given in columns 3 and 4 of Tables I–IV, while Born results for the direct and total cross sections are given in columns 1 and 2 of these tables. They were obtained as follows:

(a) Born cross sections for the $7\,^2S_{1/2}$ and $8\,^2S_{1/2}$ states have been taken from Greene and Williamson [60] who used single-particle wave functions in Hartree-Fock-Slater approximation. Their calculations extend to 136.9 and 151.1 eV, respectively, and we have extrapolated these data to 1000 eV with negligible error.

(b) The $7\,^2P_{1/2,3/2}$, $8\,^2P_{1/2,3/2}$, and $9\,^2P_{1/2,3/2}$ states are considered to evaluate cascade cross sections Q_c, and the $10\,^2P_{1/2,3/2}$-$15\,^2P_{1/2,3/2}$ states are considered to estimate cascading from higher $n\,^2P$ states. We have calculated Born cross sections for these states as $Q(nl)$ using an

TABLE I. Direct cross sections Q_D and total (cascade-including) cross sections Q_T for Rb $5\,^2S_{1/2} \rightarrow 7\,^2S_{1/2}$ electron-impact excitation. Threshold energy $E_{\text{Th}} = 3.262$ eV. Theoretical results in first Born approximation are compared to experimental total and estimated experimental direct cross sections.

Energy (eV)	Born Q_D (units of πa_0^2)	Born Q_T (units of πa_0^2)	Expt. Q_T (units of πa_0^2)	Est. Expt. Q_D (units of πa_0^2)
3.5	0.500	0.559	0.611	0.545
4	0.756	0.934	1.026	0.830
4.5	0.852	1.060	1.024	0.824
5	0.882	1.096	0.965	0.777
6	0.863	1.069	0.841	0.679
7	0.813	1.005	0.751	0.607
8	0.756	0.934	0.676	0.548
9	0.703	0.867	0.618	0.501
10	0.653	0.805	0.571	0.463
15	0.473	0.584	0.424	0.344
20	0.368	0.454	0.347	0.281
30	0.253	0.313	0.261	0.211
40	0.193	0.240	0.210	0.170
50	0.156	0.194	0.176	0.141
70	0.113	0.141	0.133	0.107
100	0.079 7	0.099 6	0.097 9	0.078 3
150	0.053 4	0.067 1	0.068 7	0.054 7
250	0.032 2	0.040 6	0.043 7	0.034 6
400	0.020 2	0.025 6	0.028 4	0.022 4
600	0.013 5	0.017 2	0.019 6	0.015 3
800	0.010 1	0.012 9	0.015 0	0.011 7
1000	0.008 10	0.010 4	0.012 2	0.009 53

TABLE II. Direct cross sections Q_D and total (cascade-including) cross sections Q_T for Rb $5\,^2S_{1/2} \rightarrow 8\,^2S_{1/2}$ electron-impact excitation. Threshold energy $E_{\mathrm{Th}} = 3.601$ eV.

Energy (eV)	Born Q_D (units of πa_0^2)	Born Q_T (units of πa_0^2)	Expt Q_T (units of πa_0^2)	Est. Expt. Q_D (units of πa_0^2)
4	0.228	0.260	0.386	0.339
4.5	0.294	0.336	0.496	0.434
5	0.323	0.369	0.471	0.413
6	0.330	0.375	0.404	0.356
7	0.316	0.358	0.344	0.304
8	0.296	0.335	0.292	0.258
9	0.276	0.312	0.254	0.225
10	0.258	0.291	0.230	0.204
15	0.188	0.212	0.175	0.155
20	0.148	0.166	0.148	0.131
30	0.102	0.115	0.112	0.099 1
40	0.077 6	0.087 5	0.090 5	0.080 2
50	0.062 7	0.070 8	0.075 9	0.067 2
70	0.045 2	0.051 1	0.058 2	0.051 5
100	0.031 8	0.036 1	0.043 1	0.038 1
150	0.021 3	0.024 2	0.030 5	0.026 9
250	0.012 9	0.014 6	0.019 5	0.017 2
400	0.008 08	0.009 21	0.012 8	0.011 2
600	0.005 40	0.006 17	0.008 85	0.007 75
800	0.004 06	0.004 64	0.006 82	0.005 96
1000	0.003 25	0.003 72	0.005 57	0.004 86

analytical Coulomb approximation recently reported by Krishnan and Stumpf [61] for alkali-metal atom excited-state–excited-state transitions. While these authors have shown that their method gives reliable results for excited-state–excited-state transitions, the method needs to be treated with caution if applied to heavy alkali-metal ^2S-^2P transitions involving the ground state because of core-polarization and spin-orbit effects. We have therefore calculated for these transitions the corresponding oscillator strengths f in analytical Coulomb approximation, divided our Born results by these f values, and multiplied them by oscillator strengths $f_{1/2}$ and $f_{3/2}$ taken from Weisheit [59] to obtain better cross section $Q(nlj)$ for fine-structure states. We note that Weisheit's results are

TABLE III. Direct cross sections Q_D and total (cascade-including) cross sections Q_T for Rb $5\,^2S_{1/2} \rightarrow 5\,^2D_{3/2}$ electron-impact excitation. Threshold energy $E_{\mathrm{Th}} = 3.186$ eV.

Energy (eV)	Born Q_D (units of πa_0^2)	Born Q_T (units of πa_0^2)	Expt. Q_T (units of πa_0^2)	Est. Expt. Q_D (units of πa_0^2)
3.5	1.087	1.110	0.942	0.860
4	1.293	1.413	1.341	1.145
4.5	1.274	1.436	1.306	1.080
5	1.203	1.374	1.216	0.993
6	1.045	1.211	1.071	0.861
7	0.911	1.065	0.939	0.750
8	0.803	0.945	0.842	0.668
9	0.718	0.847	0.768	0.607
10	0.648	0.767	0.704	0.555
15	0.434	0.518	0.494	0.386
20	0.326	0.391	0.385	0.299
30	0.217	0.262	0.265	0.205
40	0.163	0.197	0.202	0.156
50	0.131	0.158	0.164	0.126
70	0.093 3	0.113	0.119	0.091 7
100	0.065 3	0.079 3	0.084 4	0.064 8
150	0.043 5	0.053 0	0.056 8	0.043 6
250	0.026 1	0.031 9	0.034 2	0.026 2
400	0.016 3	0.020 0	0.021 4	0.016 4
600	0.010 9	0.013 4	0.014 3	0.010 9
800	0.008 16	0.010 0	0.010 8	0.008 17
1000	0.006 53	0.008 04	0.008 62	0.006 53

TABLE IV. Direct cross sections Q_D and total (cascade-including) cross sections Q_T for Rb $5\,^2S_{1/2} \rightarrow 6\,^2D_{3/2}$ electron-impact excitation. Threshold energy $E_{\mathrm{Th}} = 3.557$ eV.

Energy (eV)	Born Q_D (units of πa_0^2)	Born Q_T (units of πa_0^2)	Expt. Q_T (units of πa_0^2)	Est. Expt. Q_D (units of πa_0^2)
4	0.313	0.335	0.317	0.296
4.5	0.345	0.379	0.300	0.273
5	0.336	0.373	0.283	0.254
6	0.296	0.332	0.250	0.222
7	0.258	0.292	0.223	0.197
8	0.227	0.259	0.201	0.177
9	0.203	0.231	0.182	0.159
10	0.183	0.209	0.168	0.146
15	0.122	0.141	0.120	0.104
20	0.091 8	0.106	0.093 1	0.080 4
30	0.061 3	0.071 2	0.065 0	0.055 9
40	0.046 0	0.053 6	0.049 9	0.042 9
50	0.036 8	0.043 0	0.040 7	0.034 9
70	0.026 3	0.030 8	0.029 5	0.025 2
100	0.018 4	0.021 6	0.020 8	0.017 8
150	0.012 3	0.014 4	0.013 9	0.011 9
250	0.007 38	0.008 68	0.008 37	0.007 12
400	0.004 62	0.005 44	0.005 24	0.004 45
600	0.003 08	0.003 63	0.003 50	0.002 97
800	0.002 31	0.002 73	0.002 63	0.002 23
1000	0.001 85	0.002 18	0.002 11	0.001 78

in very good agreement with experiments [62,63] and other theoretical approaches [64,65], and we thus expect our Born cross sections for the upper $n\,^2P_{1/2,3/2}$ states to be accurate within 10% at high energies. The total cross sections Q_T in Tables I–IV and Figs. 6 and 7 contain only cascading from the $7\,^2P_{1/2,3/2}$, $8\,^2P_{1/2,3/2}$, and $9\,^2P_{1/2,3/2}$ states since cascading from $n\,^2P_{1/2,3/2}$ states with $n \geq 10$ is very small. Specifically, at 1000 eV, we find that cascading from the $7\,^2P_{1/2,3/2}$, $8\,^2P_{1/2,3/2}$, and $9\,^2P_{1/2,3/2}$ states contributes 22% to $Q_T(7\,^2S_{1/2})$ while the $10\,^2P_{1/2,3/2}$-$15\,^2P_{1/2,3/2}$ states contribute only 0.5%. For $Q_T(8\,^2S_{1/2})$ the corresponding percentages are 12.7% and 1.3%, for $Q_T(5\,^2D_{3/2})$ 18.8% and 0.8%, and for $Q_T(6\,^2D_{3/2})$ 15.4% and 2.8%. Contributions to cascading from even higher $n\,^2P$ states decrease rapidly since the oscillator strengths and hence the high-energy cross sections are proportional to the inverse cube of the effective quantum number and since the lifetimes are proportional to the cube of the effective quantum number. Thus atoms in high-lying $n\,^2P$ states will increasingly travel out of the region of observation before contributing what is already a negligible amount of cascade fluorescence.

(c) For the $5\,^2D_{3/2}$ and $6\,^2D_{3/2}$ states, again we have used an analytical Coulomb approximation to obtain cross sections $Q(nl)$ and multiplied them with the statistical weight 0.4 to obtain $Q(nlj)$. While it is difficult to assess the accuracy of these calculations in a quantitative way, we note that core-polarization and spin-orbit perturbation affect D states much less than P states. We would therefore expect that the Coulomb approximation handles the transition integrals fairly well in this case.

(d) Born cross sections for $4\,^2F_{5/2}$ to $9\,^2F_{5/2}$ states have been obtained in a manner analogous to the $^2D_{3/2}$ states above. The statistical weight is $\frac{3}{7}$.

(e) Branching ratios for fine-structure transitions, needed in Eq. (1) to evaluate cascade cross sections Q_c and probably accurate within 10%, were obtained from Theodosiou [58].

D. Cross sections

Our measured total (cascade-including) cross sections Q_T are shown in Fig. 6 as Fano plots [66], that is, $Q_T E$ vs $\log_{10}(E)$. Individual data points are shown as closed circles with some typical individual error bars, obtained as the geometrical mean of the standard deviations of signals with and without atom beam. The solid curves are smooth curves through these data points, and values for the experimental Q_T in column 3 of Tables I–IV have been taken from these smooth curves. The large diamond symbol marks the result of the experimental normalization at 100.5 eV, and its error bar denotes the accuracy of absolute normalization as determined in Sec. III B. While individual error bars or, equivalently, the scatter of individual data points about the smooth solid curves indicate the statistical error of the cross-section data ($\sim$5%), the error bar attached to the diamond symbol gives the systematic, correlated error of absolute normalization (13.5%, 17%, 15%, and 24% for $7\,^2S_{1/2}$, $8\,^2S_{1/2}$, $5\,^2D_{3/2}$, and $6\,^2D_{3/2}$). Total cross sections Q_T and direct cross sections Q_D, calculated in first Born approximation (Sec. III C), are shown for comparison.

As demonstrated in Fig. 6, the agreement between our measured Q_T and our calculated first Born Q_T for the $5\,^2D_{3/2}$ and $6\,^2D_{3/2}$ states is excellent. First, the experi-

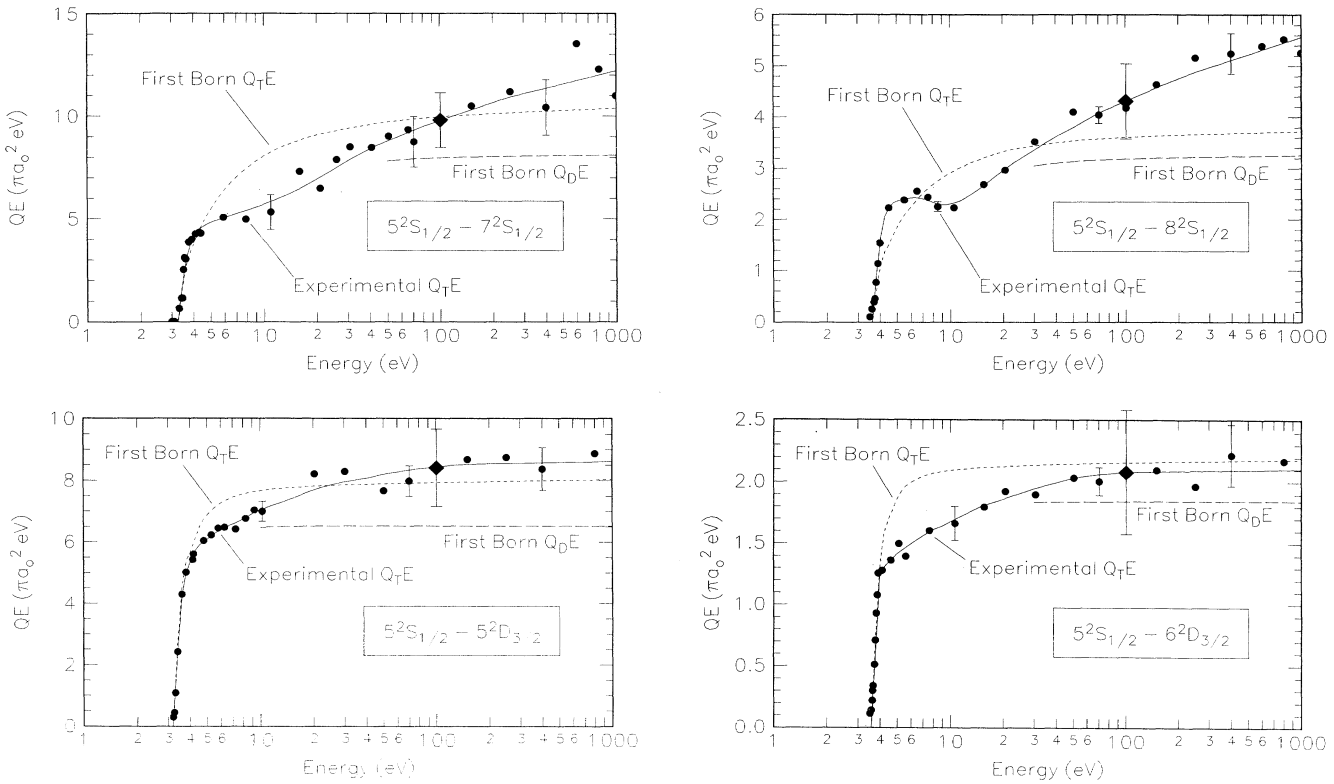

FIG. 6. Fano plots of total (cascade including) cross sections Q_T for electron-impact excitation of the Rb $7\,^2S_{1/2}$, $8\,^2S_{1/2}$, $5\,^2D_{3/2}$, and $6\,^2D_{3/2}$ states from the $5\,^2S_{1/2}$ ground state. The solid line is a smooth curve through the experimental data (●) with some typical statistical errors (70% confidence). These data are calibrated at 100.5 eV in absolute units with respect to the total cross section $5\,^2S_{1/2} \rightarrow 5\,^2P_{1/2}$ (Sec. III B). The error of the calibration point (◆) markes the accuracy of the (cross section)×(energy) scale. First Born approximations (Sec. III C) for direct and total cross sections Q_D and Q_T are shown for comparison.

mental data clearly converge to the first Born approximation for energies higher than 100 eV. Since $^2S_{1/2} \rightarrow {}^2D_{3/2}$ excitations are optically forbidden quadrupole transitions, the expected asymptotic high-energy behavior for the direct cross sections is $Q(nlj) \sim 1/E$, so the direct cross section will approach a constant in a Fano plot. $^2S_{1/2} \rightarrow {}^2P_{1/2,3/2}$ transitions are optically allowed with an asymptotic $Q(nlj) \sim f \log_{10}(CE)/E$ behavior, where f is the absorption oscillator strength and C is a constant. Thus cascading from the $^2P_{1/2,3/2}$ states could yield a finite, constant slope for EQ_T, while cascading from the F states adds only a constant. But these $^2S_{1/2} \rightarrow n\,^2P_{1/2,3/2}$ transitions with $n > 7$ have very small oscillator strengths, so EQ_T should approach a constant at high energies. This is exactly the behavior we see in the experimental Q_T in Fig. 6. Second, our measured Q_T and our calculated first Born Q_T agree very well in magnitude at high energies. For $E > 100$ eV, agreement is within 6.7% for $5\,^2D_{3/2}$ and 3.7% for $6\,^2D_{3/2}$. Of course, this agreement gives strong support to our method (Sec. III C) of obtaining first Born cross sections for direct excitation of higher D states and cascading into these states.

On the other hand, our measured total cross sections Q_T for the $7\,^2S_{1/2}$ and $8\,^2S_{1/2}$ states do not converge to first Born approximation even at energies as high as 1000 eV. As is clearly shown in Fig. 6, the experimental EQ_T keeps rising with little tendency to approach a constant at high energies. This is certainly no experimental artefact; while residual-gas excitation (optically allowed molecular transitions) or filter leakage from the strong rubidium resonance lines could add to the total signal, producing a straight Fano line at high energies, such systematic errors can safely be ruled out in this measurement. Note again that we take data with atom beam on and off. While this is experimentally more difficult than simply chopping the electron beam, it eliminates directly the contribution from residual-gas excitation. The rubidium resonance lines have thresholds at 1.560 eV ($^2P_{1/2}$; 794.76 nm) and 1.589 eV ($^2P_{3/2}$; 780.03 nm), and the total cross section for Rb ^2P rises to $70.3\pi a_0^2$ [37] at 3.0 eV. From the scatter of the zero signal obtained at this energy from the $7\,^2S_{1/2}$ state (threshold 3.262 eV) via the 740.82-nm line we estimate that a possible resonance-line contribution to $Q_T(7\,^2S_{1/2})$ at 1000 eV is no more than about 3%. Also, $EQ_T(5\,^2D_{3/2})$ observed via the 761.89-nm line approaches a constant, showing no contribution from an optically allowed transition, and $EQ_T(8\,^2S_{1/2})$ observed via the 615.96-nm line has a slope comparable to that of $EQ_T(7\,^2S_{1/2})$. Thus the basic observation that $Q_T(5\,^2D_{3/2})$ and $Q_T(6\,^2D_{3/2})$ converge to the first Born approximation for energies higher than 100 eV, and that $Q_T(7\,^2S_{1/2})$ and $Q_T(8\,^2S_{1/2})$ do not converge even at an

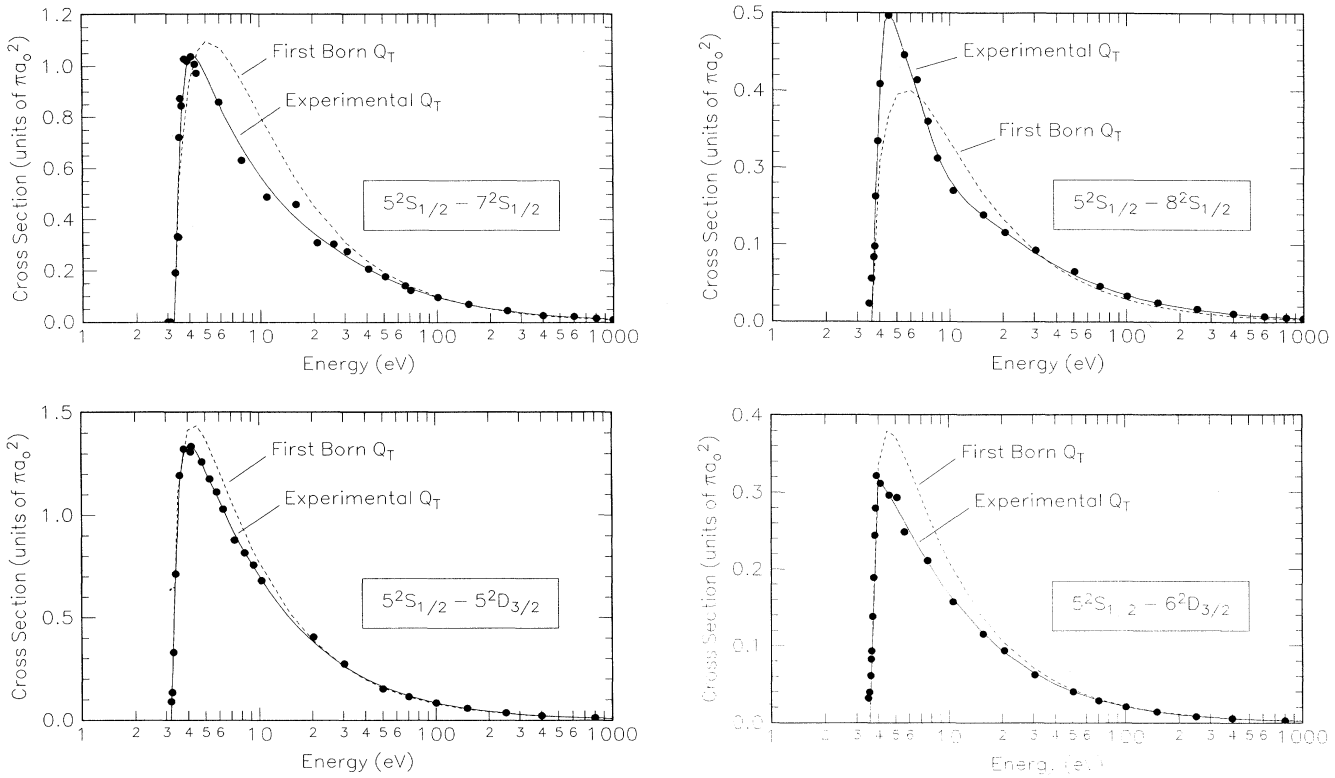

FIG. 7. Total (cascade including) cross sections Q_T for electron-impact excitation of the Rb $7\,^2S_{1/2}$, $8\,^2S_{1/2}$, $5\,^2D_{3/2}$, and $6\,^2D_{3/2}$ states from the $5\,^2S_{1/2}$ ground state. Experimental data (●) are compared with calculations in first Born approximation.

energy of 1000 eV, can be seen experimentally correct just by comparing the results in Fig. 6 and the wavelengths of the transitions involved. Furthermore, the finite slope of EQ_T for the $7\,^2S_{1/2}$ and $8\,^2S_{1/2}$ states can certainly not be attributed to cascading for the same reasons we have given above for the $5\,^2D_{3/2}$ and $6\,^2D_{3/2}$ states, and the comparison of first Born EQ_D and EQ_T in Fig. 6 clearly demonstrates this. We note, nevertheless, that even in the case of the $7\,^2S_{1/2}$ and $8\,^2S_{1/2}$ states first Born theory renders a fair order-of-magnitude estimate. Also, Born theory predicts correctly that EQ_D or EQ_T approach a constant at high energies much more rapidly for $S \rightarrow D$ than for $S \rightarrow S$ transitions.

The question now is, why do these $S \rightarrow S$ transitions converge so slowly towards first Born theory? The answer is certainly not to consider possible improvement by the second Born approximation. Hertel and Rost [67], while studying the sodium $3S \rightarrow 4S$ excitation in second Born approximation, have clearly shown that at energies of 500 eV first and second Born approximation coincide. On the other hand, the matrix element $\langle R_{n'l'}(r)|j_0(kr)|R_{nl}(r)\rangle$ that describes an $S \rightarrow S$ transition in first Born approximation with single-electron wave functions (k is the magnitude of the momentum transfer of the colliding electron and r is the radial coordinate of the atomic valence electron) couples an initial-state wave function $R_{nl}(r)$ with a final-state wave function $R_{n'l'}(r)$ that are both finite at the origin. Also, the zero-order spherical Bessel function $j_0(kr)$ is finite at the origin. This situation is unique to $S \rightarrow S$ transitions, and therefore wave functions should be used that account sufficiently for inner-shell effects like the polarization of the Rb^+ core. Of course, it can be speculated that the nonrelativistic Born theory will never describe well heavy alkali-metal $S \rightarrow S$ transitions in the 100–1000-eV regime. If the inner part of the atom should matter that much, then these excitations are made by a continuum electron that may come close enough to the nucleus to be accelerated to relativistic speeds. Nevertheless, as a first step to tackle high-energy electron $S \rightarrow S$ scattering for heavy alkali-metal atoms, we suggest that recently developed methods [40] to obtain accurate wave functions for heavy alkali-electron scattering be extended to these $7\,^2S_{1/2}$ and $8\,^2S_{1/2}$ states and new Born calculations be carried out.

Figure 7 shows total cross sections Q_T versus energy. All cross sections have steep onsets at threshold, clearly resolved with our energy resolution of 0.25 eV, rise to a sharp maximum located about 1 eV above threshold, and fall off rapidly. Qualitatively, this is what one would expect for optically forbidden $S \rightarrow S$ and $S \rightarrow D$ transitions. The agreement between our experimental data and our first Born calculations is fairly good for the $5\,^2D_{3/2}$ and $6\,^2D_{3/2}$ states even at low and intermediate energies. In this context we note that for rubidium, oscillator strengths are 1.02 for $5S \rightarrow 5P$, 0.04 for $5P \rightarrow 5D$, and

0.03 for $5P \rightarrow 6D$ [68]. Since the latter oscillator strenghts are very small, coupling of these $5D$ and $6D$ states to the ground state should not be significantly altered by virtual two-step excitations via the intermediate $5P$ state. We would therefore not expect dramatic differences between calculations in first and second Born approximation for these $5\,^2D_{3/2}$ and $6\,^2D_{3/2}$ states. As for the $7\,^2S_{1/2}$ and $8\,^2S_{1/2}$ states, it has been established above that experimental data do not converge to first Born theory at high energies. Thus any agreement in Fig. 7 between experiment and theory for these S states is probably fortuitous.

IV. COMPARISON AND CONCLUSION

To our knowledge, no other experiments have been reported thus far that deal with electron-impact excitation of higher states of heavy alkali-metal atoms covering the energy range from threshold to 1000 eV. Zapesochnyi and Shimon [69], in extending on earlier work by the latter [70], have measured, from threshold to 30 eV, absolute total cross sections for the 740.8-, 616.0-, 761.9-, and 620.6-nm spectal lines originating from the $7\,^2S_{1/2}$, $8\,^2S_{1/2}$, $5\,^2D_{3/2}$, and $6\,^2D_{3/2}$ states. These authors obtained for the maximum of the total cross sections $0.309\pi a_0^2$, $0.0679\pi a_0^2$, $0.378\pi a_0^2$, and $0.113\pi a_0^2$ with an error 30–35 %. Dividing these values by branching ratios (Sec. III B) 0.392, 0.338, 0.470, and 0.618 yields maximum level cross sections $0.789\pi a_0^2$, $0.201\pi a_0^2$, $0.805\pi a_0^2$, and $0.183\pi a_0^2$ for the $7\,^2S_{1/2}$, $8\,^2S_{1/2}$, $5\,^2D_{3/2}$, and $6\,^2D_{3/2}$ states. In comparison, our maxima are $1.03\pi a_0^2$, $0.50\pi a_0^2$, $1.34\pi a_0^2$, and $0.32\pi a_0^2$ with statistical error $\sim 5\%$ and calibration errors 13.5%, 17%, 15%, and 24% (Sec. III B). On the other hand, the locations of the maxima, ~ 0.9 eV above threshold, agree very well. For the ratio $Q_T(\text{max})/Q_T(30\text{ eV})$ Zapesochnyi and Shimon find ~ 3 while our measurements give ~ 4 for the $^2S_{1/2}$ states and ~ 5 for the $^2D_{3/2}$ states. We note that the early work of Zapesochnyi and co-workers on electron–alkali-metal-atom collisions has frequently been found [43] to disagree with modern experiments by more than the stated errors.

As for higher-state excitation in other alkali-metal atoms, Zajonc and Gallagher [45] have studied electron-impact excitation of the Li $3S$, $4S$, $3D$, and $4D$ states, and Stumpf and Gallagher [17] have measured the Na $3S \rightarrow 3D$ cross section. In both papers it is found that the cross sections for the D states in Fano plots rise to a maximum somewhat below 100 eV and then decrease towards a constant high-energy value. We do not find this behavior for the Rb $5\,^2D_{3/2}$ and $6\,^2D_{3/2}$ states. Displayed in a Fano plot, the cross sections for these states approach a constant at high energies from below, not from above. Whether this is a characteristic difference between electron excitation of light and heavy alkali-metal atoms should be investigated in future experiments in cesium. Consistent with our findings, Zajonc and Gallagher also observe that the Li $3S$ and $4S$ cross sections converge more slowly to first Born theory at high energies than the Li $3D$ and $4D$ cross sections. However, their $S \rightarrow S$ cross sections appear to have converged at 1000 eV, while ours do not. At low energies, Gallagher and co-workers [17,45] find broad maxima for D-state excitation. In the present work, however, the shape of the cross sections is quite similar for $S \rightarrow S$ and $S \rightarrow D$ transitions, showing sharply peaked maxima in both cases. As stated in Sec. II C, we have carefully measured the transmission of the interference filters. A mutual influence of spectral lines at 615.96 nm ($8\,^2S_{1/2} \rightarrow 5\,^2P_{3/2}$) and 620.63 nm ($6\,^2D_{3/2} \rightarrow 5\,^2P_{1/2}$), 740.82 nm ($7\,^2S_{1/2} \rightarrow 5\,^2P_{3/2}$) and 761.89 nm ($5\,^2D_{3/2} \rightarrow 5\,^2P_{1/2}$) is less than 0.1% and negligible.

Some insight into the discrepancies between higher-state excitation in the light alkali-metal atoms lithium and sodium and the present work in rubidium can be gained by studying the experimental results of Phelps and Lin [16] for higher-state excitation in sodium and by Phelps *et al.* [46] in potassium. In sodium, Phelps and Lin find broad maxima, flattening with increasing principal quantum number n, for the excitation cross sections of D states, while the cross sections of S states are sharply peaked at threshold. This is consistent with the results of Gallagher and co-workers [17,45] described above. In potassium, however, Phelps *et al.* [46] observe that D-states cross sections for $n > 4$ also show sharp threshold peaks. This is consistent with our results in rubidium. On the other hand, the excitation cross sections for S and D states of potassium still have markedly different shapes, while our experiment yields very similar shapes for S- and D-state excitation. We would therefore conclude that state-specific information, that is, not only principal quantun number n but also orbital angular momentum quantum number l, is more and more suppressed with increasing nuclear charge Z in the relative shape of higher-state alkali-metal excitation cross sections. In other words, while higher-state electron excitation of a light alkali-metal atom is essentially a two-electron problem, with one electron characterized by well-defined bound states in a frozen-core potential, higher-state excitation of a heavy alkali-metal atom appears to be more a collective process that involves the entire atom.

ACKNOWLEDGMENTS

We are indebted to our undergraduate students Mark Dexter, Rich Alfa, Curt Martin, and Russ Lawrence for their invaluable help in building the experimental apparatus. We also wish to thank Professor K. Becker, Professor B. Bederson, and Professor A. Gallagher for many stimulating discussions and continued interest in this work. We are especially grateful to Professor C. Theodosiou for sending us unpublished results on transition probabilities and branching ratios for alkali-metal fine-structure transitions, to Professor W. Baylis and Professor H. Stroke for valuable hints on oscillator strengths of heavy alkali-metal atoms, and to Uma Krishnan for her help in the Born calculations. This work was supported by the National Science Foundation under Grant No. RII-8902065.

[1] D. L. Moores and D. W. Norcross, J. Phys. B **5**, 1482 (1972).
[2] A. Kasdan, T. M. Miller, and B. Bederson, Phys. Rev. A **8**, 1562 (1973).
[3] C. K. Kwan, W. E. Kauppila, R. A. Lukaszew, S. P. Parikh, T. S. Stein, Y. J. Wan, and M. S. Dababneh, Phys. Rev. A **44**, 1620 (1991).
[4] W. Gehenn and E. Reichert, Z. Phys. **254**, 28 (1972).
[5] M. Eyb and H. Hofmann, J. Phys. B **8**, 1095 (1975).
[6] T. Shuttleworth, W. R. Newell, and A. C. H. Smith, J. Phys. B **10**, 3307 (1977).
[7] P. J. O. Teubner, S. J. Buckman, and C. J. Noble, J. Phys. B **11**, 2345 (1978).
[8] S. K. Srivastava and L. Vušković, J. Phys. B **13**, 2633 (1980).
[9] B. Jaduszliwer, P. Weiss, A. Tino, and B. Bederson, Phys. Rev. A **30**, 1255 (1984).
[10] P. J. O. Teubner, J. L. Riley, M. J. Brunger, and S. J. Buckman, J. Phys. B **19**, 3313 (1986).
[11] X. L. Han, G. W. Schinn, and A. Gallagher, Phys. Rev. A **42**, 1245 (1990).
[12] T. Y. Jiang, C. H. Ying, L. Vušković, and B. Bederson, Phys. Rev. A **42**, 3852 (1990).
[13] E. A. Enemark and Alan Gallagher, Phys. Rev. A **6**, 192 (1972).
[14] H. Hafner, Phys. Lett. **43A**, 275 (1973).
[15] B. Stumpf, K. Becker, and G. Schulz, J. Phys. B **11**, L639 (1978).
[16] J. O. Phelps and C. C. Lin, Phys. Rev. A **24**, 1299 (1981).
[17] B. Stumpf and A. Gallagher, Phys. Rev. A **32**, 3344 (1985).
[18] W. Jitschin, S. Osimitsch, H. Reihl, H. Kleinpoppen, and H. O. Lutz, J. Phys. B **17**, 1899 (1984).
[19] X. L. Han, G. W. Schinn, and A. Gallagher, Phys. Rev. A **38**, 535 (1988).
[20] S. J. Buckman and P. J. O. Teubner, J. Phys. B **12**, L583 (1979).
[21] P. J. O. Teubner, J. E. Furst, M. C. Tonkin, and S. J. Buckman, Phys. Rev. Lett. **46**, 1569 (1981).
[22] P. J. O. Teubner, J. E. Furst, and J. L. Riley, Aust. J. Phys. **35**, 501 (1982).
[23] I. V. Hertel and W. Stoll, J. Phys. B **7**, 583 (1974).
[24] H. W. Hermann, I. V. Hertel, W. Reiland, A. Stamatović, and W. Stoll, J. Phys. B **10**, 251 (1977).
[25] B. Jaduszliwer, R. Dang, P. Weiss, and B. Bederson, Phys. Rev. A **21**, 808 (1980).
[26] G. F. Hanne, Cz. Szmytkowski, and M. van der Wiel, J. Phys. B **15**, L109 (1982).
[27] H. W. Hermann and I. V. Hertel, Z. Phys. A **307**, 89 (1982).
[28] B. Jaduszliwer, G. F. Shen, J.-L. Cai, and B. Bederson, Phys. Rev. A **31**, 1157 (1985).
[29] J. J. McClelland, M. H. Kelly, and R. J. Celotta, Phys. Rev. Lett. **56**, 1362 (1986).
[30] R. E. Scholten, T. Anderson, and P. J. O. Teubner, J. Phys. B **21**, L473 (1988).
[31] J. J. McClelland, M. H. Kelly, and R. J. Celotta, Phys. Rev. A **40**, 2321 (1989).
[32] M. Zuo, T. Y. Jiang, L. Vušković, and B. Bederson, Phys. Rev. A **41**, 2489 (1990).
[33] P. J. Visconti, J. A. Slevin, and K. Rubin, Phys. Rev. A **3**, 1310 (1971).
[34] B. Jaduszliwer and Y. C. Chan, Phys. Rev. A **45**, 197 (1992).
[35] W. Gehenn and E. Reichert, J. Phys. B **10**, 3105 (1977).
[36] M. Klewer, M. J. M. Beerlage, and M. J. Van der Wiel, J. Phys. B **12**, L525 (1979).
[37] S. T. Chen and A. C. Gallagher, Phys. Rev. A **17**, 551 (1978).
[38] P. Naβ, M. Eller, N. Ludwig, E. Reichert, and M. Webersinke, Z. Phys. **11**, 71 (1989).
[39] F. Eschen, G. F. Hanne, K. Jost, and J. Kessler, J. Phys. B **22**, L455 (1989).
[40] U. Thumm and D. W. Norcross, Phys. Rev. A **45**, 6349 (1992).
[41] U. Thumm and D. W. Norcross, Phys. Rev. Lett. **67**, 3495 (1991).
[42] U. Thumm and D. W. Norcross, Phys. Rev. A **47**, 305 (1993).
[43] D. W. O. Heddle and J. W. Gallagher, Rev. Mod. Phys. **61**, 221 (1989).
[44] C.E. Moore, *Atomic Energy Levels,* Natl. Bur. Stand. (U.S.) Circ. No. 467 (U.S. GPO, Washington, DC, 1958), Vol. 2.
[45] A. Zajonc and A. Gallagher, Phys. Rev. A **20**, 1393 (1979).
[46] J. O. Phelps, J. E. Solomon, D. F. Korff, and C. C. Lin, Phys. Rev. A **20**, 1418 (1979).
[47] J. V. Kennedy, Valerie P. Myerscough, and M. R. C. McDowell, J. Phys. B **10**, 3759 (1977).
[48] J. Mitroy, I. E. McCarthy, and A. T. Stelbovics, J. Phys. B **20**, 4827 (1987).
[49] D. H. Madison, K. Bartschat, and R. P. McEachran, Bull. Am. Phys. Soc. **37**, 1134 (1992).
[50] P. O. Taylor, Ph.D. thesis, University of Colorado, 1972. Available through University Microfilms, Inc., Ann Arbor, Michigan.
[51] M. Lapp and L. P. Harris, J. Quant. Spectrosc. Radiat. Transfer **6**, 169 (1966).
[52] H. Pauly, in *Atomic and Molecular Beam Methods,* edited by G. Scoles (Oxford University Press, New York, 1988), Vol. 1, pp. 87–89.
[53] C. E. Theodosiou, Phys. Rev. A **30**, 2881 (1984).
[54] C. Tai, W. Happer, and R. Gupta, Phys. Rev. A **12**, 736 (1975).
[55] J. Marek and P. Muenster, J. Phys. B **13**, 1731 (1980).
[56] W. Hogerforst and S. Svanberg, Phys. Scr. **12**, 67 (1975).
[57] S. Svanberg and P. Tsekeris, Phys. Rev. A **11**, 1125 (1975).
[58] C. E. Theodosiou (private communication).
[59] J. C. Weisheit, Phys. Rev. A **5**, 1621 (1972).
[60] T. J. Greene and W. Williamson, At. Data Nucl. Data Tables **14**, 161 (1974).
[61] U. Krishnan and B. Stumpf, At. Data Nucl. Data Tables **51**, 151 (1992).
[62] E. Caliebe and K. Niemax, J. Phys. B **12**, L45 (1979).
[63] L. N. Shabanova and A. N. Khlyustalov, Opt. Spektrosk. **56**, 205 (1984) [Opt. Spectrosc. (USSR) **56**, 128 (1984)].
[64] D. Hofsaess, Z. Phys. A **281**, 1 (1977).
[65] J. Migdalek and W. E. Baylis, Can. J. Phys. **57**, 1708 (1979).
[66] U. Fano and A. R. P. Rau, *Atomic Collisions and Spectra* (Academic, New York, 1986), p. 53.
[67] I. V. Hertel and K. A. Rost, J. Phys. B **4**, 690 (1971).
[68] J. Migdalek and W. E. Baylis, Can. J. Phys. **57**, 1708 (1979).
[69] I. P. Zapesochnyi and L. L. Shimon, Opt. Spektrosk. **20**, 944 (1966) [Opt. Spectrosc. (USSR) **20**, 525 (1966)].
[70] L. L. Shimon, Opt. Spectrosc. (USSR) **17**, 12 (1964).